Performance of Nanotube-based Ceramic Composites: Modeling and Experiment

NASA Glenn Research Center
Grant # NAG3-2668

Final Report

for the program period
October 9, 2001 – October 8, 2004

W. A. Curtin, B. W. Sheldon, and J. Xu
Division of Engineering, Brown University, Providence, RI
Tel: 401-863-1418 ; e-mail: curtin@engin.brown.edu

Executive Summary

The excellent mechanical properties of carbon-nanotubes are driving research into the creation of new strong, tough nanocomposite systems. In this program, our initial work presented the first evidence of toughening mechanisms operating in carbon-nanotube-reinforced ceramic composites using a highly-ordered array of parallel multiwall carbon-nanotubes (CNTs) in an alumina matrix. Nanoindentation introduced controlled cracks and the damage was examined by SEM. These nanocomposites exhibit the three hallmarks of toughening in micron-scale fiber composites: crack deflection at the CNT/matrix interface; crack bridging by CNTs; and CNT pullout on the fracture surfaces. Furthermore, for certain geometries a new mechanism of nanotube collapse in "shear bands" was found, suggesting that these materials can have multiaxial damage tolerance. The quantitative indentation data and computational models were used to determine the multiwall CNT axial Young's modulus as 200-570 GPa, depending on the nanotube geometry and quality.

We subsequently aimed at in-depth analyses and modeling of the deformation processes. A 3d FEM model of the indentation cracking was generated, using a cohesive zone model to represent nanotube bridging, matrix cracking, and residual stresses simultaneously. Comparison of the model to experimental data on crack growth versus load leads to derived values for the nanotube bridging toughness of ~5 MPa-$m^{1/2}$, a 10x increase over that toughness of the matrix alone. The analyses also provides for estimate of the nanotube strength in the range of 15-25 GPa and for the nanotube/matrix sliding resistance of 40-190 MPa. The high apparent sliding resistance is surprising, since the nanofibers are carbon-based and should slide easily.

To understand the nature of the pullout forces, we then investigated the pullout behavior of fractured multiwall nanotubes. Molecular Dynamics simulations on multiwall tubes showed that the fractured end of an interior nanotube wall resists pullout through the surrounding intact nanotube walls with a high force that dominates the resistance due to surface energy alone. As a consequence of this effect, the pullout force is independent of the embedded length of fractured nanotube, which is in contrast to standard interfacial friction models for sliding behavior. To obtain friction-like sliding requires heterogeneity along the nanotube length, such as distributed residual pressures due to confinement of the nanotube within a rough matrix tube. These basic results indicate that the macroscopic models for composite fracture must be modified to account for non-friction–like behavior.

To understand some features of the fracture of the pure nanoporous Alumina, we investigated the as-fabricated and heat-treated matrices in the absence of any nanotube additions. The Young.s modulus, hardness, and fracture toughness of highly-ordered nanoporous alumina were measured by nanoindentation and Vicker's microindentation. A finite element model accurately accounting for the anisotropy and pores was used to extract the Young's modulus and hardness from the indentation data. The principle results were (i) accounting for the pores, the Young's modulus of the alumina material is 140 GPa, which is unaffected by heat treatment to 650C, (ii) an increase in the hardness from 5.2 GPa to 6.3 GPa after heat treatment, and (iii) a strong decrease in fracture toughness from 3.4 to 0.4 MPa-m^1/2. When indented on the top of the specimen, i.e. parallel to the pores, the nanopores undergo a collapse or buckling phenomenon rather than fracture, suggesting damage-tolerant behavior at the nanoscale in these materials.

1. Scientific Achievements

1.a Experimental Discoveries

The discovery of carbon nanotubes (CNTs) has sparked considerable interest in their use as reinforcements in various matrix materials to impart stiffness, strength, and toughness [1-6]. Novel mechanical tests on individual CNTs [2,3] in polymer matrices and atomistic calculations [4-6] suggest that CNTs have high elastic moduli, approaching 1 TPa, and exceptional tensile strengths, in the range of 20-100 GPa. The transference of these properties into correspondingly good mechanical properties in actual composites depends on many other *in-situ* features: the CNT/matrix interfacial adhesion, the CNT/matrix interfacial sliding behavior after any decohesion [7], the interwall sliding within multiwall nanotubes, and the fracture behavior and fracture strength statistics of CNTs, among others. These features have proven difficult to assess, even qualitatively, in real systems due to the difficulty in (i) fabricating well-controlled CNT composites and (ii) testing such systems. Although some enhanced mechanical properties in polymer matrices have been reported [8-12] and toughening in a polycrystalline alumina with dispersed single-walled CNTs has very recently been reported [13], there has been no direct evidence regarding the deformation, damage, and toughening mechanisms at the nanoscale. Furthermore, whether composite fracture and damage mechanics at the nanoscale differs from that at the micron-scale due to the near-atomic-scale geometry of the material is simply unknown. In Year 1, we showed direct evidence that the critical deformation and damage modes associated with toughening in "standard" micron-scale ceramic matrix composites do occur in a CNT-reinforced ceramic matrix material [14]. Furthermore, the nanocomposite systems exhibit entirely new deformation mechanisms, both in the composites and in the reinforcing fibers.

An SEM of the top surface of the 90 μm -thick composite is shown in **Figure 1.** Such specimens were subjected to nanoindentation, with a Berkovitch indenter and a cube-cornered indenter, on the top and side of the nanocomposite.

A crack induced by top indentation of the 20 μm -thick sample is shown in **Figure 2**, demonstrating the phenomenon of crack deflection. **Figures 3** shows the separated crack surfaces in the 90 μm -thick sample indented on the side. CNTs are observed to bridge the gap between the surfaces over a large fraction of the crack surface. **Figure 4** show one such surface in which the CNTs clearly project out of the fracture surface, demonstrating CNT pullout. **Figure 5** shows that, in systems with larger-diameter/thin-wall nanotubes, the deformation upon top indentation is accommodated by lateral buckling or collapse of the nanotubes in shear bands rather than cracking, demonstrating multiaxial damage tolerance in these systems.

1.b Continuum Modeling of Experiments to Extract Mechanical Properties

Here, we are interested in the nanotube crack bridging phenomenon and associated toughening, and thus restrict our attention to the results from indentation on the side surface, which generated cracks running transverse to the nanotube fiber axis. **Figure 3** shows the separated crack surfaces on the side of the 90-μm-thick sample for different loading levels. CNTs bridge the gap in all the range of applied load. The bridging is consistent with crack deflection at the matrix/nanotube interface found previously: perpendicular cracks reach the CNT/matrix interface and deflect longitudinally along

the interface rather than propagating through the CNTs. Our goal here is to deduce the toughening associated with the nanotube bridging.

Crack growth is restrained by the fracture toughness of the matrix and the closure forces exerted by the bridging CNTs, which together represent the toughness of the composite. At equilibrium the driving and restraining forces balance all along the crack perimeter so that [16]

$$\chi \frac{P}{c^{3/2}} + Y\sigma_{mr}V_m\sqrt{c} = K_m + \frac{2}{\sqrt{\pi c}}\int_0^c \frac{rp(u(r))}{\sqrt{c^2 - r^2}}dr \tag{2}$$

where K_m is the fracture toughness of the matrix, $p(u)$ is the nanofiber bridging traction, which is a function of the half crack opening at position r relative to the center of the crack, and $\sigma_{mr}V_m$ is the effective porous matrix residual stress, with χ and Y as loading and geometry parameters. The work per unit area done by the bridging traction, G_b, can be expressed in terms of the bridging tractions as

$$G_b = 2\int_0^{u_b} p(u)du \tag{3}$$

where u_b is one-half the maximum crack opening of the bridging nanofibers under the current loading. The maximum toughening due to fiber bridging occurs once the opening reaches a value $u_b = u^*$ at which the bridging tractions become zero. The bridging toughness K_b can be expressed in terms of the work done by fiber bridging, G_b, as

$$K_b = \sqrt{\frac{G_b E_c}{1 - \nu_c^2}} \tag{4}$$

where E_c and ν_c are the effective Young's modulus and Poisson's ratio of the composite, respectively. The composite fracture toughness is the sum of bridging and matrix toughness, $K_c = K_b + K_m$, and our goal here is to obtain K_b, which follows from determination of the crack-surface traction $p(u)$ as a function of crack opening u.

We use a combined analytical and numerical model to determine the crack-surface traction. Following previous approaches in which bridging fibers slide with an interfacial sliding resistance τ, we model the bridging force $p(u)$ as a function of half crack opening u in the presence of residual stress in the composite as

$$p(u) = \frac{E_f V_f}{2}\left\{\left(\frac{\sigma_c}{E_c} - \frac{\sigma_{mr}}{E_m}\right) + \left[\left(\frac{\sigma_c}{E_c} + \frac{\sigma_{mr}}{E_m}\right)^2 + \frac{16\tau}{RE_f}u\right]^{1/2}\right\} \tag{5}$$

where E_f and E_m are there Young's modulus of nanotube and matrix, respectively, V_f and V_m are the nanotube and matrix volume fraction, respectively, R is the radius of the nanotubes. We thus simplify the situation by assuming $\sigma_c = 0$ so that Eq. 5 reduces to

the model developed by Marshall, Cox, and Evans and widely used in the literature. To determine the crack-opening displacement u and to permit natural extension of the matrix crack, we have developed a finite element model that employs both the cohesive model of Eq. 5 for the fiber bridging and a cohesive zone model for the matrix cracking. Making use of symmetry, a 60°-wedge model was developed as illustrated in **Figure 6**. The x-z surface at $y=0$, perpendicular to the nanotube axis, is the plane of crack growth in this geometry and contains a cohesive zone designed to permit matrix crack growth [17]. Specifically, an initial small-radius, free surface region is surrounded by a region in which special 2d rod elements perpendicular to the crack plane are employed as cohesive elements to permit crack growth, with the normal traction T_m and corresponding displacement jump, u, across the interface given by [19]

$$T_m = \frac{\sigma_{\max}}{u_n} u e^{1-\frac{u}{u_n}} \tag{6}$$

where σ_{max} is the maximum interfacial normal tensile strength and u_n is a characteristic critical opening length. For such a cohesive zone law, the normal work of fracture G and the associated matrix fracture toughness K_m are

$$G = e\sigma_{\max} u_n = G_m V_m = \frac{K_m^2 (1-\nu_m^2)}{E_m} V_m \quad , \tag{7}$$

where E_m and ν_m are the Young's modulus and Possion ratio of the matrix, respectively. For simplicity, we also include the matrix residual stress into the cohesive tractions. The total traction in the nanotube bridging area is

$$T(u) = p(u) + T_m(u) - \sigma_{mr} V_m \quad , \tag{10}$$

an example of which, for relevant material parameters, is shown in **Figure 6**.

The simulations are then carried out as follows. For a chosen interfacial shear resistance τ, the displacement U is incremented until the corresponding lateral force F is such that the indentation load $P(F)$ reaches the experimental value for a desired crack length c, given in Table 2. The FEM model naturally forms a bridged matrix crack with surface length c' that differs from the measured value c. Based on the difference between c and c', the value of τ is adjusted and the procedure repeated until self-consistency is obtained. Thus, the interfacial shear resistance is used as the one adjustable parameter to match the model to each experimentally-measured load-crack data point.

Figure 7 shows the predicted stress distribution and crack front in the cohesive zone for the composite material for the largest load/longest crack case. In this case, there is an unbridged region between the indent and the start of CNT bridging (see Figure 3). The matrix crack grows outward but does not maintain a precise penny shape. The crack bridging tractions show a concentration near the crack surface at the end of the bridging zone, with lower values into the depth of the crack. This suggests that the broken CNTs exist preferentially near the crack surface, so that surface observations do not provide a complete picture of the deformation. Figure 3, showing

surface damage but some sub-surface bridging, is in qualitative agreement with this aspect of the calculations.

The fiber bridging toughness is calculated from the numerical results as follows. Upon adjusting τ so that the model and experimental matrix crack and bridging lengths match for a given applied load, we extract the crack opening at the end of the bridging zone (for the small and medium crack lengths, this corresponds to the corner of the indent) from the simulation. This crack opening is then taken as u^*, the maximum bridging opening for the nanotubes, and is input into Eq. 4 along with the bridging law of Eq. 5 and the value of τ to calculate the bridging work. The toughness contribution is then calculated from Eq. 3. When the bridging zone extends back to the corner of the indent, the value of u^* is a lower-bound value: nanotube fracture is not yet observed at this opening. Thus, the corresponding toughness values are also lower bounds.

Using the experimental data and parameters in Table 1 and 2, the predicted bridging fracture toughness, interfacial frictional stress and maximum half opening for the composites are shown in Table 4. The fracture toughness is about 5 MPa-$m^{1/2}$, recalling that the lower load data provide lower bounds. Similar values of ~5 MPa-$m^{1/2}$ are obtained for the bridging toughness of the 20-μm thick specimens (not presented here because bridging was not observed directly). This value of toughening is substantially larger than the matrix toughness alone (0.4 MPa-$m^{1/2}$), demonstrating the significant role of fiber bridging on toughening in these nanocomposites.

With a maximum crack opening and τ calculated, the bridging law can be used to estimate the tensile strength of the CNTs. The bridging laws deduced from the three load levels are shown in **Figure 8** along with the maximum openings and corresponding CNT tensile strengths. As an aside, note that the work done by bridging is the area under each of these curves. The tensile strength values of the CNTs range about 15-25 GPa, consistent with the measurement by other researchers and lower then theoretical values, presumably due to the lack of high order in our CNTs.

1.c Nanoscale Modeling of Nanotube Pullout

An important issue in developing CNT-based composites is load transfer between the matrix and the nanotubes and between the internal shells of individual MWCNTs. Load transfer plays several roles, but most important are its effects on composite strength and toughness. Assuming frictional sliding with an interfacial shear sliding stress tau, unidirectional tensile strength and work-of-fracture scale as $\tau^{1/m}$ and $\tau^{-(m-1)/m+1}$, respectively, where m is the Weibull modulus describing the statistical distribution of nanotube strengths. Therefore, independent of the reference nanotube strength (e.g. average tensile strength at some specified gauge length), composite fracture depends on the strength and nature of the friction, and can approaches zero for low τ. The precise origins of CNT sliding behavior and the magnitude of the sliding force are thus key to properly understanding and optimizing CNT composite behavior.

Here, we consider the sliding behavior of multiwall carbon nanotubes with the inner wall(s) broken and being pullout of the outer walls. We demonstrate that the static "frictional" sliding in carbon nanotubes is not really frictional in nature for two related reasons: (i) the force to pull out the inner walls of a nanotube is independent of the embedded length and (ii) in broken-end, or uncapped, nanotubes, the force is controlled

entirely by deformations associated with effects at the embedded "broken" end of the inner nanotube walls. Our results are in quantitative agreement with explicit experiments on the direct pullout of inner nanotube walls from outer nanotube walls.

The molecular dynamics (MD) method was used to simulate nanotube pullout for a variety of geometries at near zero temperature. Double-wall MWCNTs in the Zigzag and Armchair configurations were generated, with the inner wall tube protruding out from the end of the outer wall. The embedded end of the inner wall was either capped, by connecting dangling C bonds appropriately, or uncapped, corresponding to a cleanly fractured inner nanotube, as shown schematically in **Figures 9 a,b**. A nanotube diameter of about d=16 Å and typical lengths of L=80-100 Å were used for most of the calculations. The Tersoff-Brenner potential was used to represent the intrawall C-C bonding [22]. The interwall interaction was modeled by the classical Lennard-Jones potential $E(r)=4e[(r_0/r)^{12}-(r_0/r)^6]$ with r_0=3.468 Å and e=2.86 meV. The range of this potential was taken to be 20 nm, so that the long-range effects of the van der Waals portion of the potential were appropriately included. In the simulation, the inner tube was pulled out in displacement increments of 0.1-0.2 A, with relaxation to equilibrium after each increment. To assess the sliding associated with no end effects, the geometry shown in **Figure 9c** was also investigated, where a narrow ring at the center of the outer tube is held fixed. For a given applied displacement of the inner nanotube wall, we measure the applied pullout force F and calculate the pullout stress σ=F/A, where A is the effective cross section of the inner tube, $A = 2\pi dt$, where t= 3.48 A is the nominal interwall spacing.

Figure 10 shows the measured pullout stress as a function of sliding distance for defect-free armchair and zigzag nanotubes. There is an initial loading portion, as the nanotubes are stretched and the free end on the inner nanotube enters the interior of the outer nanotube, followed by a "sliding" regime as the inner tube is gradually pulled out of the outer tube. In the sliding regime, the force is generally oscillatory, with the periods of oscillation very close to the relevant quasi-periodicity along the nanotube axis, 2.17 Å for zigzag and 1.0 Å for the armchair. Moreover, there is a markedly different magnitude of the pullout force for the different end conditions: the uncapped ("fractured") end exhibits a pullout force three to four times larger than that of the capped end. Both calculations with an embedded end show much larger forces than in the case with no embedded end (**Figure 9c**). Examination of the stresses along the uncapped nanotube explicitly demonstrates that the stresses are high at the position of the embedded end of the inner nanotube. Thus, the "sliding" friction behavior in broken MWCNTs is controlled by the shear strength of the embedded end defect sliding against the outer walls.

The high level of force in the uncapped embedded nanotube can be understood by observing that the fractured nanotube end splays outward due to the force unbalance induced by the broken bonds, as shown in Figure **9e**. The interaction of this splayed end with the confining walls of the outer nanotube requires application of a comparatively large force to induce motion. For the capped end, the absence of the splaying eliminates any end effects, and the pullout force is proportional to the surface energy. The forces calculated here for capped nanotubes are consistent with the MD simulations performed by Legoas *et al.* [24] in their study of CNT oscillators. The results with no embedded end also demonstrate that the sliding is not controlled by the "fractured" end of the *outer* nanotube wall, as postulated previously, because the broken end splays outward.

We have compared our MD results against the experimental data on pullout or telescoping of the inner walls of individual MWCNTs reported by Akita et. al [25] and Yu et al.. [26]. In Akita's telescoping experiments, the outer layers of MWCNTs were cut using an electrical breakdown technique. The cut outer layers were pulled out from an end-capped inner wall with an outer diameter of 5 nm. The force for extraction was measured to be a constant at 4.2 nN. Our calculation for the capped nanotubes, scaled to the experimental diameter, is 4.4 nN, in excellent agreement the experimental results. The nanotube pullout experiments done by Yu et al. are similar to those by Akita et.al., but the nanotubes are large in diameter and the outermost shells were broken by extension. The pullout forces are listed in **Table 5** along with our calculated results scaled to the appropriate diameters. The data of Yu et al. agree well with the predictions of the forces for the uncapped nanotube ends. The calculations performed here thus rationalize the notable differences in pullout forces between the two sets of data: one set corresponds to capped ends and the other to uncapped ends.

1.d Experiments on Nanoporous Alumina

The behavior of the nanoporous Alumina deduced from our initial work was interesting. Also, to deduce the toughening due to the nanotubes required knowledge of the matrix toughness. The anodized alumina is amorphous and can undergo changes after low-temperature annealing, as occurs during processing of the nanotube composites. Thus, we performed some experiments and analysis to determine the properties of this material.

The nanoporous Alumina was subjected to nanoindentation and microindentation both in the as-processed state and after heat-treating at 650C for the time used in the nanotube deposition process.

Figure 11 shows the infrared spectrum before and after heat treatment. The broad peak at higher wavenumbers decreases substantially, indicating a loss of water in the structure. However, the X-ray spectrum was unaltered, indicating no fundamental change in the amorphous structure.

Figure 12 shows the data for modulus and hardness before and after annealing, as measured by indentation on the side of the sample at various positions and analyzed using standard formulae appropriate for isotropic materials. The change in modulus after annealing is negligible, consistent with the absence of any structural change. The hardness increases by approximately 20%, presumably due to the loss of water upon annealing. The modulus and hardness vary through the cross-section, presumably due to a variation in pore diameter through the cross-section, as discussed below.

Because of the uniaxial alignment of the pores, the standard formula for modulus is not appropriate. Furthermore, it must be demonstrated that the variations in **Figure 12** are due only to the pore diameter variations. **Figure 13** shows a schematic of the procedure used to relate the unloading modulus measured in the indentation experiments to the elastic modulus of the porous material. By an iterative process of varying the input alumina modulus and comparing to the data at various points through the cross-section with varying pore size, we have been able to obtain the actual alumina modulus. The data is shown in **Figure 14** along with the pore diameter. The deduced modulus is independent of position, indicating that the alumina properties are uniform in the cross-section.

Finally, measurement of crack lengths upon nano and microindentation on the side of the sample were made, and used to deduce the fracture toughness. The as-received material has a rather high toughness of 3.4 MPa-m^1/2, although the lower hardness and compressibility (ability to accommodate substantial volume changes by pore collapse) may invalidate the use of the standard formula. The annealed material shows much more brittle behaviour, as shown by comparison of **Figures 15a,b, and c**. The corresponding toughness is quite low, 0.4 MPa-m^1/2.

The low toughness in the annealed material has important implications for the nanotube composites. First, these results show that the annealed matrix material is indeed quite brittle, and thus serves as an excellent "model" ceramic matrix material, in spite of the amorphous nature and low modulus of the material relative to alpha-alumina. Second, as a result, the toughness of ~5 MPa-m^1/2 reported above for the composites then demonstrates that the nanotubes can impart reasonable toughness to the nanoscale composite system. Although 5 MPa-m^1/2 is not a substantial toughness, the goal here was not to obtain a tough material but rather to demonstrate the operation of toughening mechanisms in nanoceramic composites.

1.e Summary

Excellent and unique technical work was performed in this project. We demonstrated that toughening mechanisms known to operate in "standard" micron-scale CMCs also operate in nanotube-based CMCs. This result suggests that many of the existing theories for CMC performance can be applied to nanotube-CMCs, and that engineering of the nanotube properties, interfaces, and residual stresses is feasible for improving and/or optimizing nanotube-CMC performance, and especially toughness. A new mechanism of damage tolerance, nanotube collapse under loading on the composite coating top surface, was demonstrated. Combined with the toughening due to nanotube bridging of cracks when indented on the side of the specimen, these results indicate that nanoceramic composites may have multiaxial damage tolerance.

New analysis methods were developed to interpret the experimental results and extract intrinsic material properties such as modulus, nanotube strength, and interfacial sliding resistance. Although these methods require further refinement, and more experiments should be analyzed, the basic ideas are now in the literature.

Finally, nanotube sliding behaviour is expected to be quite different from standard micron-scale fiber behaviour. Our simulations of nanotube pullout demonstrate this fundamental difference. At the same time, these computations quantitatively explain recent experimental results on sword-and-sheath pullout from multiwall nanotubes. If composites are indeed made from high-quality multiwall nanotubes, the special sliding behaviour of nanotubes may require new approaches to understanding the toughening and other mechanical behaviour. We believe that the nanotubes employed in our experiments were not perfect in internal structure, and that this turns out, in fact, to be a distinct advantage. Some strength loss is compensated by much greater interface sliding that may be frictional, leading to good toughness. Thus, the experiments and modelling here together suggest that control of nanotube structure, i.e. perfection in the nanotube walls, may permit a range of properties to be obtained, perhaps with some optimum obtainable.

In spite of the technical success of this project, it was terminated early with only 2/3 of the original funding received. Thus, some of the interesting and novel aspects of

our work could not be pursued further. The investigation of alternative nanotube materials was also not possible due to termination of funding.

2. Publications and Presentations

All of the above work has been published in peer-reviewed journals. Further details can thus be gleaned from those papers. Note that these papers have received excellent attention in the field, and that our work as been reported in *invited* talks at the American Ceramic Society annual meeting (2003), Carbon 2004, High-Temperature CMC (2004), and a number of universities including U. Connecticut, RPI, U. Tokyo, Tohuku U., and Brown U.

1. Z. Xia*, L. Reister, W. A. Curtin, B. Sheldon, J. Xu, "Direct Observation of Toughening Mechanisms in Carbon Nanotube Ceramic Matrix Composites", Acta Mater. 52, 931-944 (2004).
This paper was featured as a Research Highlight in Materials Today

2. Z. Xia, W. A. Curtin, B. W. Sheldon, "Fracture Toughness of Highly-ordered Carbon Nanotube/Alumina Nanocomposites", J. Eng. Matl. Tech. – Transaction of the ASME **126**, 238-244 (2004).

3. Z. Xia, L. Reister, B. W. Sheldon, W. A. Curtin, J. Liang, A. Yin, and J. M. Xu, "Mechanical Properties of Highly Ordered Nanoporous Anodic Alumina Membranes", Rev. Adv. Mater. Sci. **6**, 34-40 (2004).

4. Z. Xia and W. A. Curtin, "Pullout Forces and Friction in Multiwall Carbon Nanotubes", Phys. Rev. B **69**, 233408 (2004).
This paper was selected for on-line publication in Nanomaterials

5. B. W. Sheldon and W. A. Curtin, "Nanoceramic Composites: Tough to Test", Nature Materials **3**, 505-506 (2004).
This paper is a commentary on toughening in nanotube ceramics, invited based on our research work in this program.

6. W. A. Curtin and B. W. Sheldon, "Review: Ceramic and Metal Nanocomposites", Materials Today, November (2004).
This paper was invited due to our research results in this program.

3. References:

1. Iijima, S. Helical Microtubules of Graphitic Carbon. *Nature* **354**, 56-58 (1991).
2. Yu, M. F., Lourie, O., Dyer, M. J., Molor, K., Kelly, T. F., & Ruoff, R. S. Strength and breaking mechanism of multiwalled carbon nanotubes under tensile loads. *Science* **287**, 637-640 (2000)
3. Wagner, H. D., Lourie, O., Feldman, Y. & Tenne, R. Stress-induced fragmentation of multiwall carbon nanotubes in a polymer matrix. *App. Phy. Lett.* **72**, 188-190 (1998).
4. Yakobson, B. I. & Avouris, P. Mechanical properties of carbon nanotubes. *Topics in Applied Physics* **80**, 287-327 (2001)
5. Nardelli M. B., Yakobson B. I. & Bernholc J. Brittle and ductile behavior in carbon nanotubes. *Phys. Rev. Lett.* **81**, 4656-4659 (1998).
6. Belytschko, T., Xiao, S. P., Schatz, G. C., & Ruoff, R. S. Atomistic simulation of nanotube fracture. *Phys. Rev. B* **65**, #235430 (2002).
7. Curtin, W. A. Stress-strain response of brittle matrix composites. *Encyclopedia of Composites*, eds. A. Kelly and C. Zweben, (Elsevier, Holland) 2000.
8. Lourie, O. & Wagner, H. D. Evidence of stress transfer and formation of fracture clusters in carbon nanotube-based composites. *Comp. Sci. Tech.* **59**, 975-977 (1999).
9. Andrews, R., Jacques, D., Rao, A. M., Rantell, T. & Derbyshire, F. Nanotube composite carbon fibers. *App. Phys. Lett.* **76**, 2868-2870 (1999).
10. Qian, D., Dickey, E. C., Andrews, R. & Rantell, T. Load transfer and deformation mechanisms in cabon nanotube-polystyrene composites. *App. Phy. Lett.* **76**, 2868-2870 (2000).
11. Allaoui, A., Bai, S., Cheng, H. M. & Bai, J. B. Mechanical and electrical properties of a MWNT/epoxy composite. *Comp. Sci. Tech.* (in press, 2002).
12. Peigney, A., Flahaut, E., Laurent, Ch., Chastel, F. & Rousset, A. Aligned carbon nanotubes in ceramic-matrix nanocomposites prepared by high-temperature extrusion. *Chem. Phys. Lett.* **352**, 20-25 (2002).
13. Zhan G., Kuntz J. D., Wan J. and Kukherjee A.K., Nature Materials, 2,38-42 (2003).
14. Xia Z., Riester L., Curtin W. A., Li H., Sheldon B. W., Liang, J. Chang B. and Xu J.,2003, "Direct observation of toughening mechanisms in carbon-nanotube ceramic matrix composites", to appear in Acta Mater. 2004.
15. Pharr G. M., 1998, "Measurement of mechanical properties by ultra-low load indentation," Mater. Sci. Eng., **A253**, pp.151-159.
16. Paris P.C. and Sih G.C., 1965, "Stress analysis of cracks, pp.30-83, in Fracture toughness testing and its applications, ASTM STP 381, American Society of Testing and Materials, Philadelphia, PA.
17. Xia Z., Curtin W.A. and Sheldon B.W., 2003, "A New Method to Evaluate the Fracture Toughness of Thin Films," Acta Mater., submitted.
18. Xia Z., and Curtin W. A., 2001, "Life prediction of titanium MMCs under low-cycle fatigue, "Acta Mater., **49,** pp.1633-1646.

19. Xu, X.P. and Needleman, A., 1993, Void nucleation by inclusion debounding in a crystal matrix," Mod. Sim. Matl. Sci. Eng., 1, pp.111-132.
20. Maniwa Y, Fujiwara R, Kira H, Tou H, Kataura H, Suzuki S, Achiba Y, Nishibori E, Takata M, Sakata M, Fujiwara A, Suematsu H., 2001, "Thermal expansion of single-walled carbon nanotube (SWNT) bundles: X-ray diffraction studies," Phy.Rev.B, **64,** #241402-1-3.
21. O'Day M.P. and Curtin W.A., 2002, "Failure of crossply ceramic-matrix composites," J.Am. Ceram. Soc., 85, pp.1553-1560.
22. Brenner D.W., Physical Review B, 42 (1990), 9458-9471
23. Girifalco L.A., Hodak M. and Lee R., Phys. Rev., 62 (2000) 13104-13110
24. Legoas S.B., Coluci V. R., Braga S.F., Coura P.Z., Dantas S.O. and Galvao D.S., Phys. Rev. Lett. 90 (2003) No.055504
25. S. Akita and Y. Nakayama, Interlayer sliding force of individual multiwall carbon nanotubes, Jpn. J. Appl. Phys. 1 42 (2003), pp. 4830-4833.
26. M.F. Yu, B.I. Yakobson and R.S. Ruoff, Controlled sliding and pullout of nested shells in individual multiwalled carbon nanotubes. Journal of Physical Chemistry B 104 37 (2000), pp. 8764-8767.

4. Tables

TABLE 1. Mechanical properties of CNTs and alumina matrix [14]

Materials	Tube diameter (nm)	Tube thickness (nm)	$E_{rr}=E_{TT}$ (GPa)	E_{zz} (GPa)	K_{Ic} (MPa-$m^{1/2}$)
Al_2O_3	-	-	140	140	0.4
CNT	56	4.5	365	570	-

TABLE 2. Indentation crack length and apparent fracture toughness (Eq.1)

Material	Maximum Load (mN)	Crack length (μm)	Impression size (μm)	Bridging length (μm)	Apparent Fracture Toughness (MPa-$m^{1/2}$)
Al_2O_3/ 30% CNT	200	8.4	3.5	4.9	1.3
	400	12.8	8.5	4.3	1.4
	650	30.3	11.1	16.2	0.6

TABLE 3. Parameters for the matrix cohesive zone

Model	Mesh size (μm)	K_{Ic} (MPa-$m^{1/2}$)	σ_m (MPa)	δ_c (μm)
Small	0.166	0.29	168	1
Medium	0.332	0.29	168	2
Large	0.665	0.29	168	4

TABLE 4. Fracture toughness of CNT nanocomposites as deduced by the finite element model

Material	Maximum Load (mN)	Crack length (μm)	Frictional stress (MPa)	Maximum half crack opening (nm)	Fracture Toughness (MPa-$m^{1/2}$)
Al_2O_3/ 30% CNT	200	8.4	195	38	>4.2
	400	12.8	170	44	>4.6
	650	30.3	40	76	4.9

TABLE 5. Pullout forces for multiwall carbon nanotubes as calculated using the atomistic model stresses scaled to the appropriate diameter and as measured experimentally by different groups.

Nanotube Diameter (nm)	Calculated Force: fractured end (nN)	Calculated Force: capped end (nN)	Measured Force (nN)	Ref.
5	21-25	**5.0**	4.2*	25
30	**124-154**	26.5	85	26
36	**149-185**	31.8	152	26

* Capped end nanotubes

Table 5.

Table 1. Mechanical properties of porous Al_2O_3 calculated by standard formula (Effective Modulus) and finite element model (FEM).

Material	Treatment, Orientation	Average Pore Diameter (nm)	Hardness H, (GPa)	Effective E, (GPa)	FEM E_{rr} or E_{zz} (GPa)	K_{Ic} (MPa-$m^{1/2}$)
20 μm-Al_2O_3	As-fabricated	37	5.0	104	93	–
	Side* Top	37	5.3	126	128	–
90 μm-Al_2O_3	As-fabricated	50**	5.2	107	74	2.4
	Side* Top	60.3	3.4	85	92	–
90 μm-Al_2O_3	Heat treatment	50**	6.8	104	75	0.28
	Side* Top	60.5	4.1	86	93	–

* in the middle of the sample

5. Figures

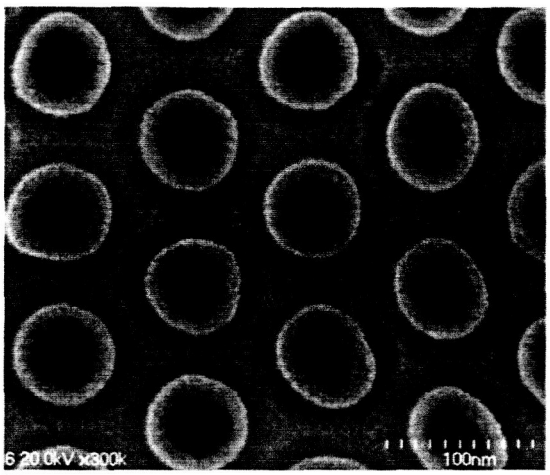

Figure 1. SEM photograph of as-fabricated CNT/ceramic composite viewed from the top, showing high degree of hexagonal order (mottled surface due to deposited conductive gold coating).

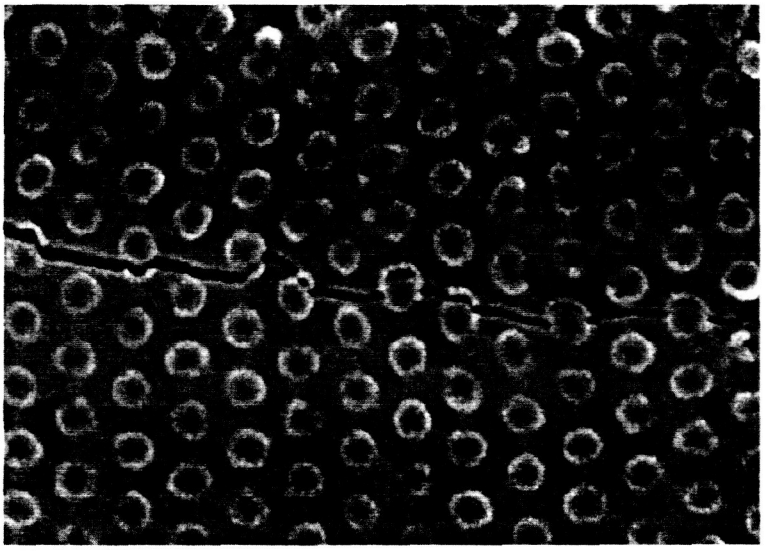

(b)

Figure 2. SEM photograph showing the crack intersection with the successive CNT/matrix interfaces and deflection around the CNTs along the interface.

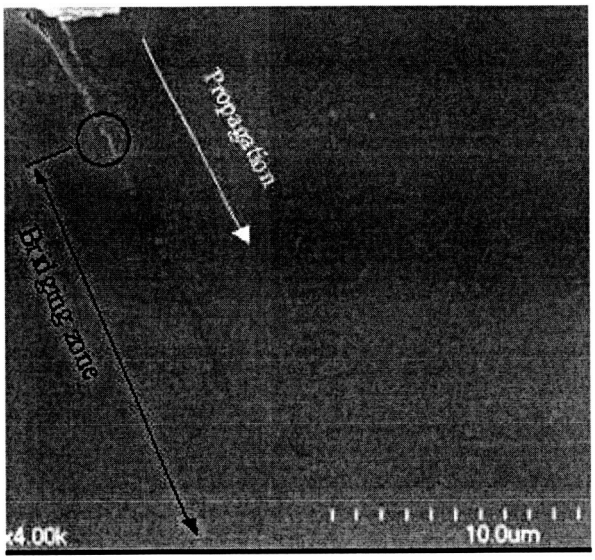

(a)

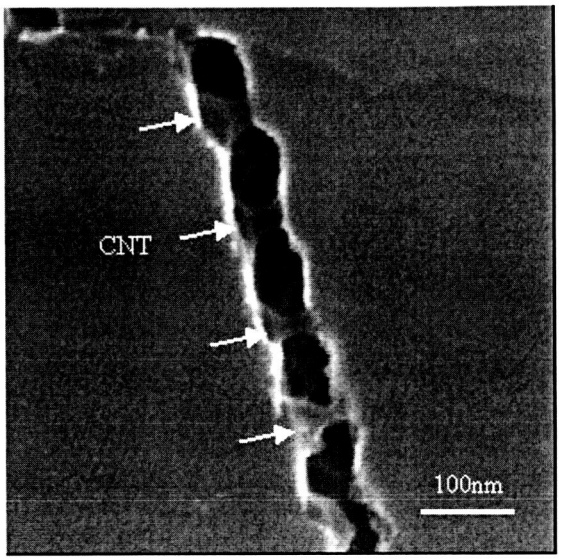

(b)

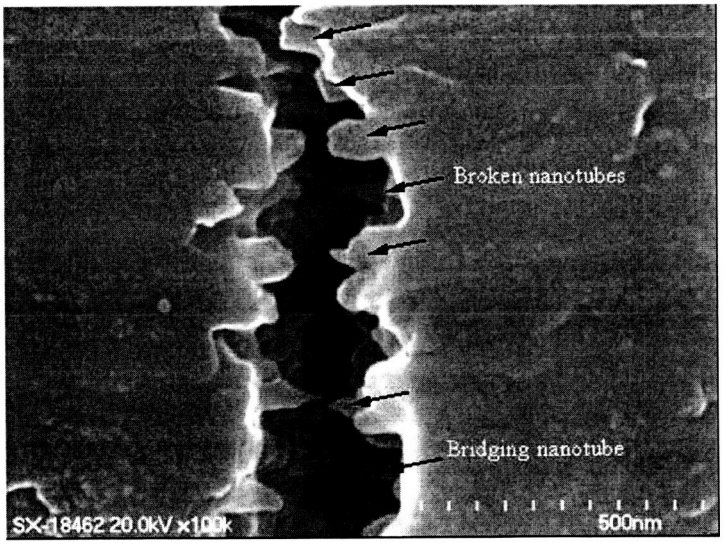

(c)

Figure 3. (a) Side indentation crack pattern on 90 μm thick sample at a load of 650mN; (b) the magnification of circled area in (a) showing bridging CNTs at a distance away from the indent; (c) magnification of the completely cracked area, showing broken nanotubes, nanotube pullout, and subsurface nanotube bridging.

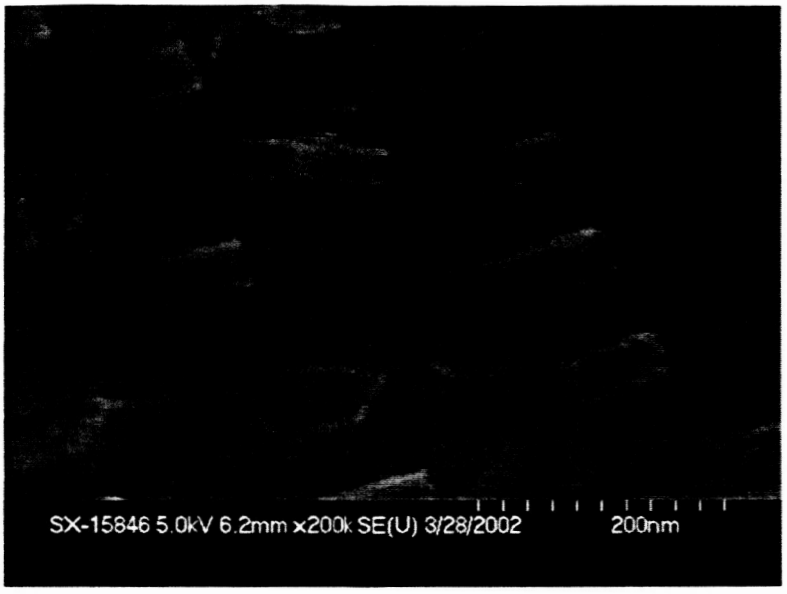

Figure 4. SEM photograph a fracture surface of the 20 μm -thick sample demonstrating CNT pullout.

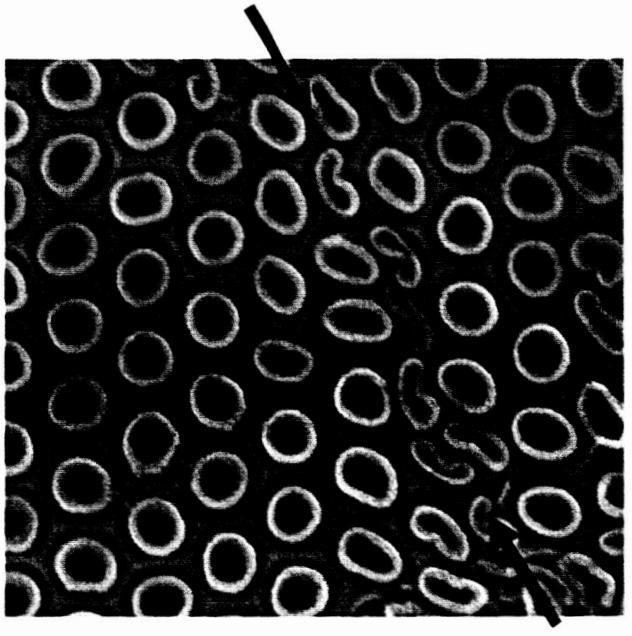

Figure 5. SEM photographs of deformation around indent in the 90 μm -thick sample showing lateral buckling or collapse of the nanotubes in one "shear band".

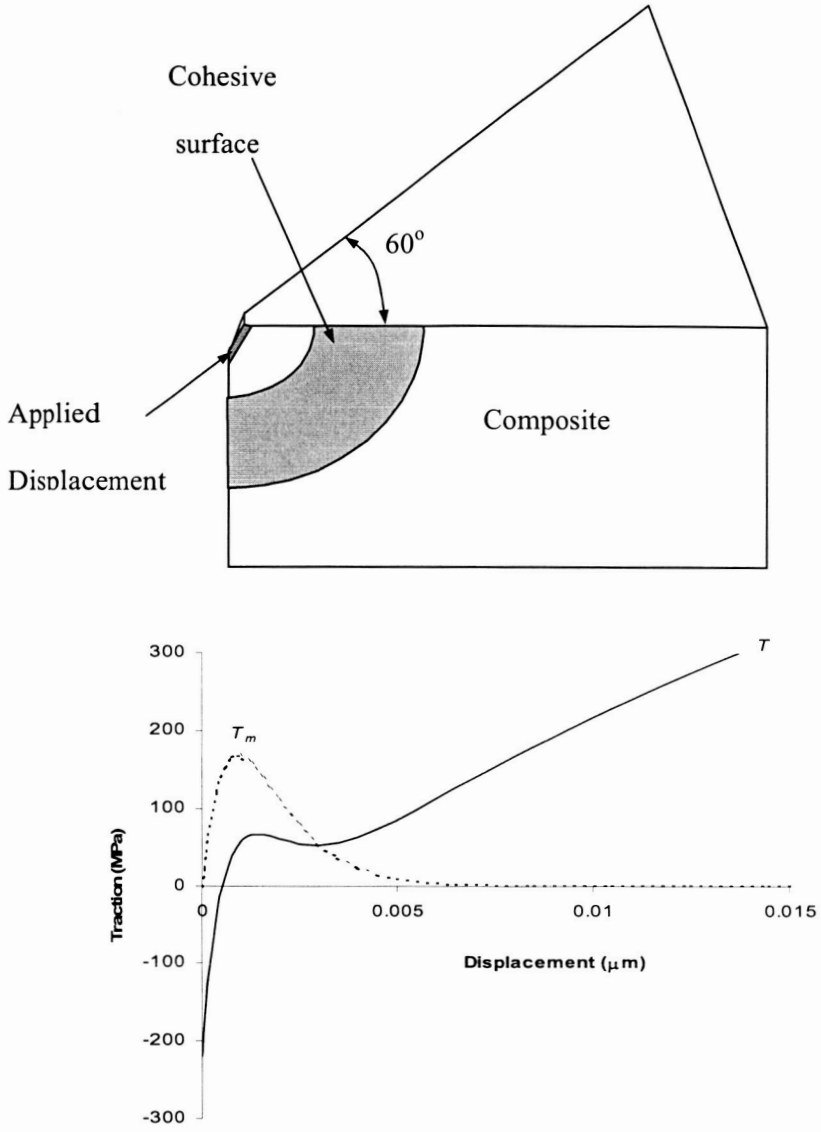

Figure 6. a) Geometry of the finite element model with cohesive zone region. b) Matrix and total tractions versus crack half-opening, for 30% CNT in Al_2O_3 matrix, with a matrix residual stress σ_{mr}=300 MPa, matrix fracture toughness of 0.4 MPa-$m^{1/2}$, and interfacial sliding stress $\tau = 40$ MPa.

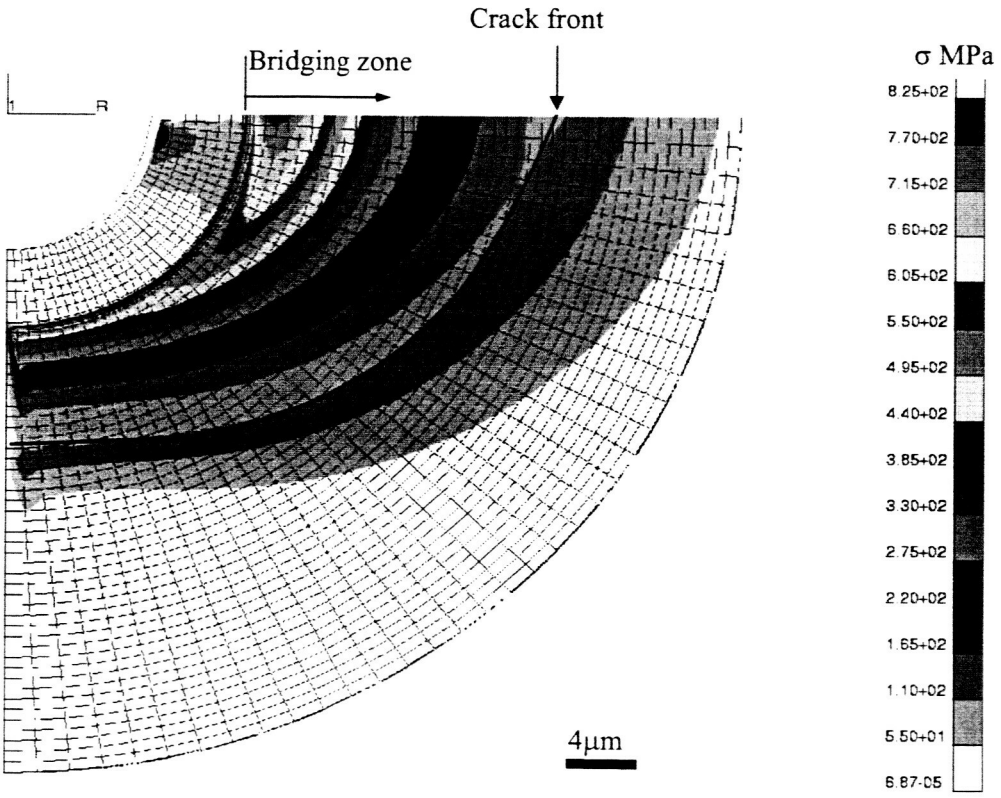

Figure 7. Stress distribution as predicted by the cohesive zone model for the largest indent crack at an applied load of 580mN.

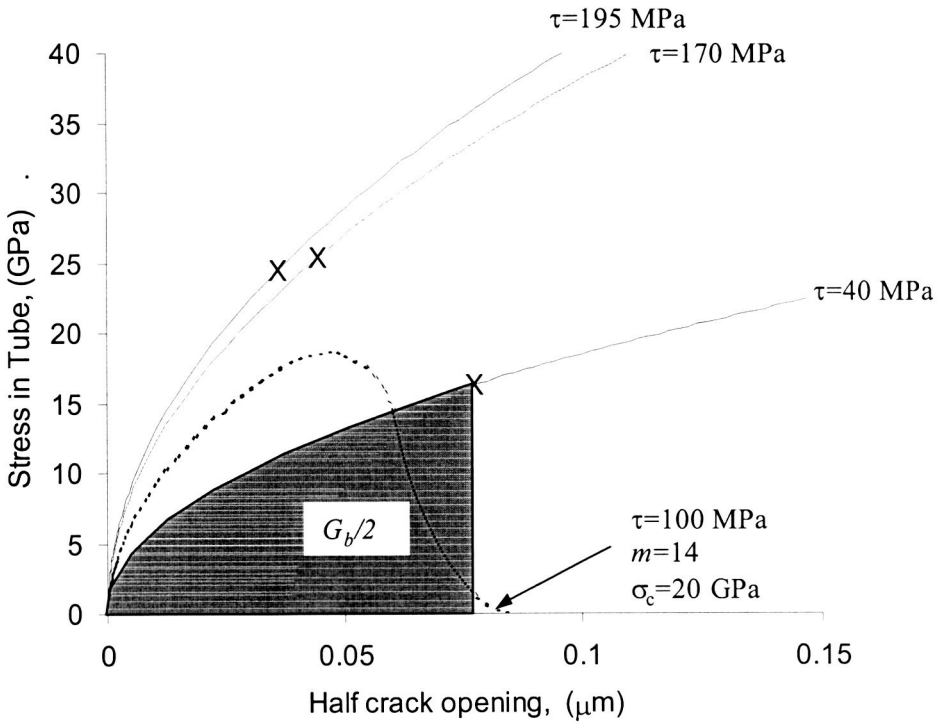

Figure 8. CNT bridging traction versus half-crack opening, for the three cases shown in Table 4. X denoting the maximum opening point and associated CNT tensile stress. The shadowed area corresponds to the bridging fracture energy (Eq. 3) to determine composite fracture toughness. The dotted line shows a possible unifying bridging law that accounts for the statistical nanotube strength [34].

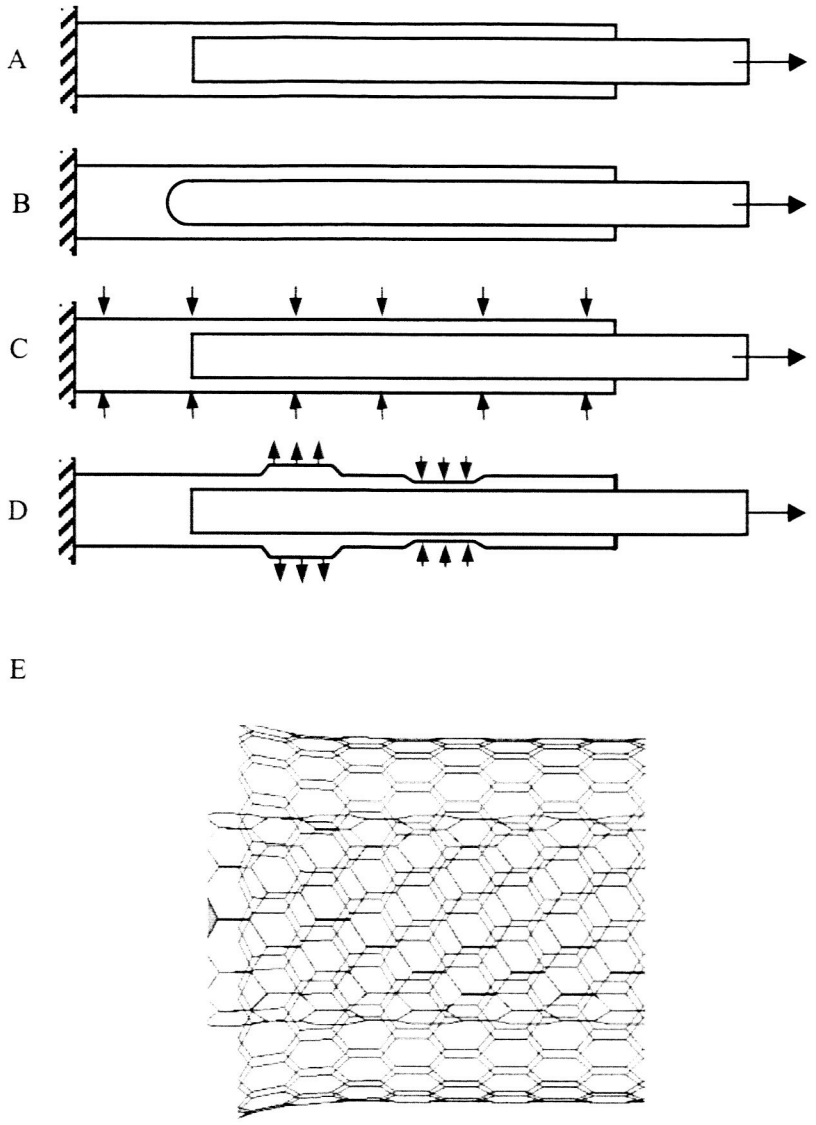

Figure 9. Schematic representation of (a) opened end nanotube pullout, (b) capped end pullout, (c) pullout with uniform pressure, (d) pullout with non-uniform pressure, (e) splayed end of broken nanotube (outer nanotube shown for clarity).

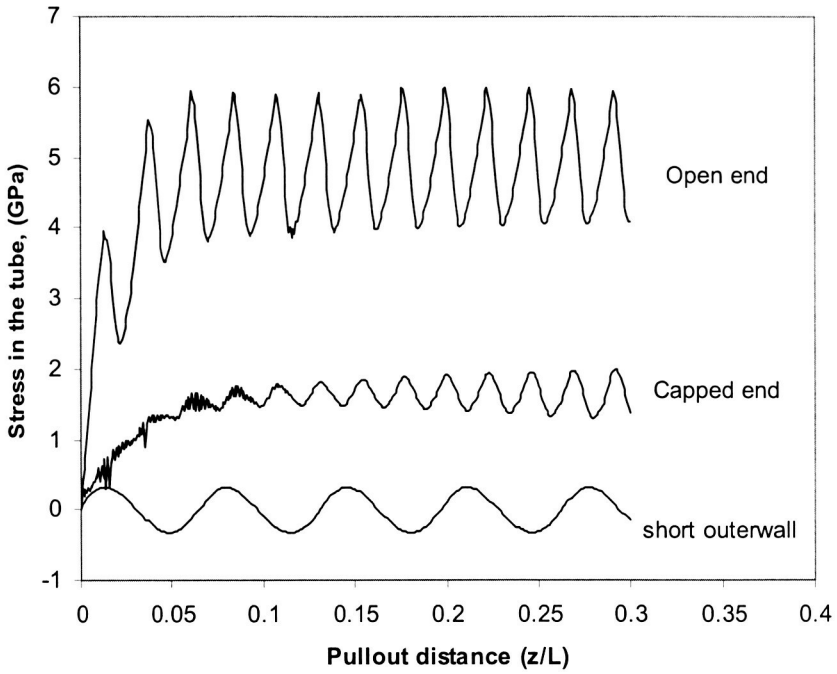

Figure 10. Pulling stress at the pulling end of the inner layers for broken (open) and capped end of double-walled zigzag nanotubes.

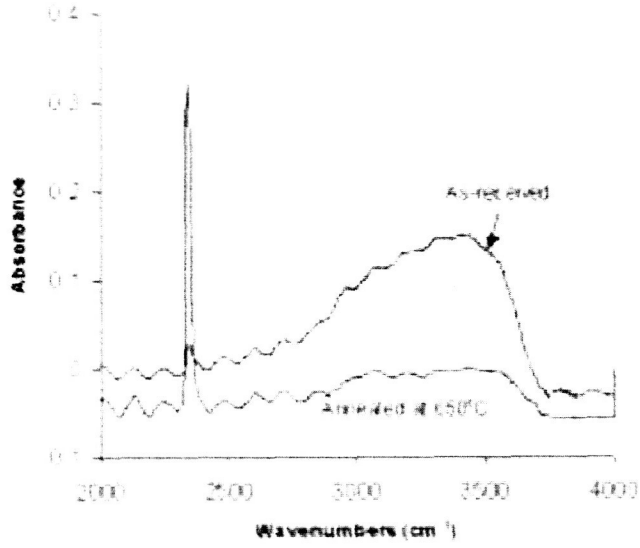

Figure 11. Infrared spectrum of as-received and annealed nanoporous anodized alumina.

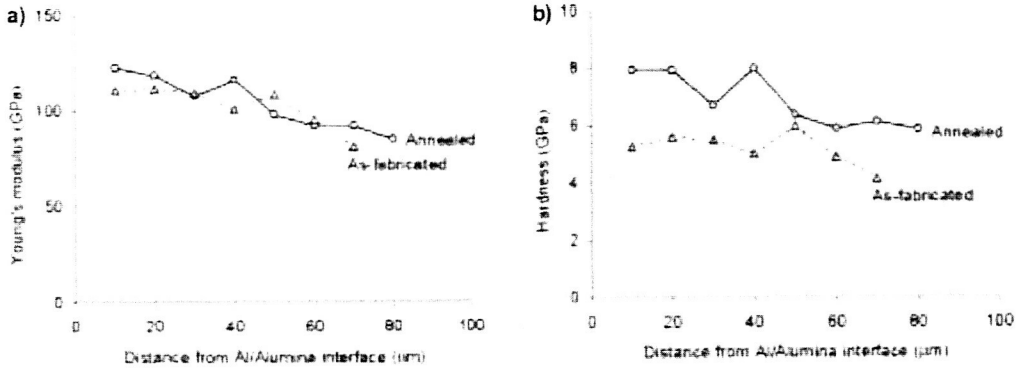

Figure 12. Modulus and hardness measured by indentation on the side of the specimen as a function of the position in the film, before and after annealing, and interpreted using standard formulae.

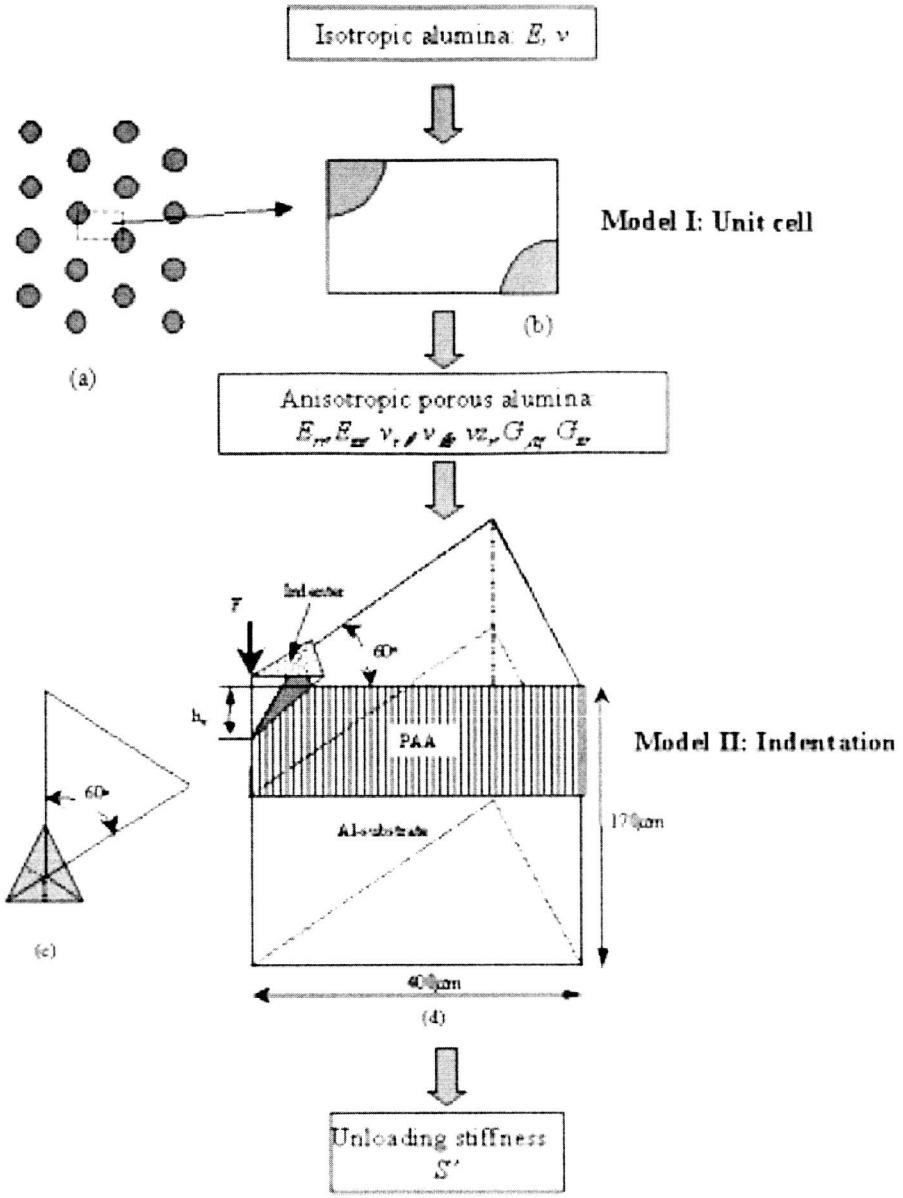

Figure 13. Schematic of multiscale computational approach used to deduce fundamental material properties from indentation experiments on the anisotropic nanoporous alumina.

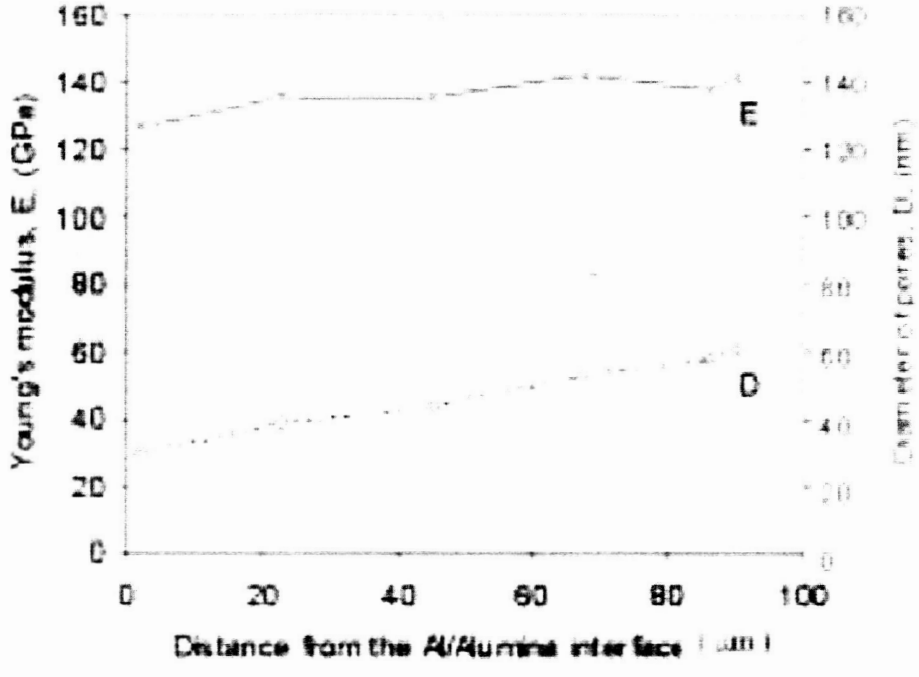

Figure 14. Young's modulus of the alumina (not including the pores) deduced from our analysis, showing independence of the position through the film. Also shown is the pore diameter versus position, which accounts for the modulus variations shown in Figure 12.

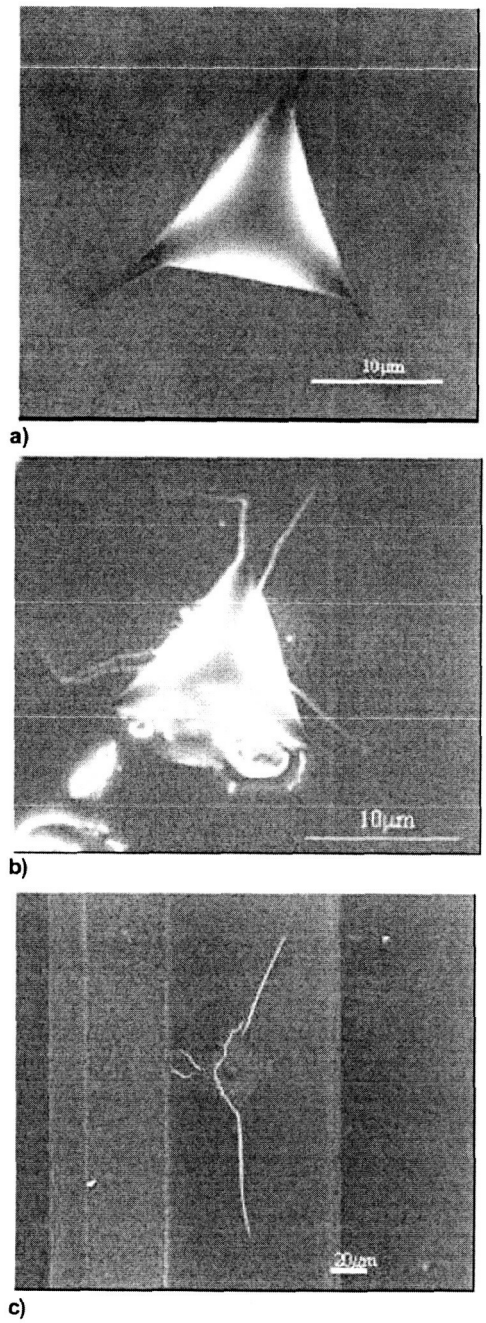

Figure 15. SEM images of indentation crack generated on porous alumina samples, (a) as-fabricated and on the side at 650 mN, (b) heat-treated and on the side at 400 mN, and (c) heat-treated and on the side by microindentation at a load of 500g.